NUCL SCI TECH (2018) 29:148
https://doi.org/10.1007/s41365-018-0477-y

Performance of beam size monitor based on Kirkpatrick–Baez mirror at SSRF

De-Chong Zhu[1,2] · Jun-Hui Yue[1] · Yan-Feng Sui[1,2] · Da-Heng Ji[1] · Jian-She Cao[1] · Kai-Rong Ye[3] · Shun-Qiang Tian[3] · Jie Chen[3] · Yong-Bin Leng[3]

Received: 2 March 2018 / Revised: 17 April 2018 / Accepted: 26 April 2018 / Published online: 3 September 2018

Abstract High-energy photon source (HEPS) is a 6 GeV ultralow emittance storage ring light source to be built in Beijing, China. Both the horizontal and vertical beam sizes of the HEPS storage ring are below 10 µm. It is a challenge to measure such a small beam size in both directions. To this end, measurement by a Kirkpatrick–Baez (KB) mirror imaging system was evaluated. A test KB system for the Shanghai Synchrotron Radiation Facility storage ring was designed and tested. Two crossed cylindrical mirrors were used to image the dipole source point. Both mirrors can be moved in and out so that the monitor is interchangeable with the original X-ray pinhole monitor. The aberration and point spread function, which would cause image blur, were evaluated. A beam-based calibration scheme was used by varying the beam size with different quadrupole settings and fitting them with the corresponding theoretical values. We updated the original X-ray camera with a new camera having a 5-µm-thick LuAG/Ce scintillator, and the imaging result shows greatly decreased image blur.

✉ Jian-She Cao
caojs@ihep.ac.cn

De-Chong Zhu
zhudc@ihep.ac.cn

1 Key Laboratory of Particle Acceleration Physics and Technology, Institute of High Energy Physics, Chinese Academy of Sciences, Beijing 100049, China

2 University of Chinese Academy of Sciences, Beijing 100049, China

3 Shanghai Institute of Applied Physics, Chinese Academy of Sciences, Shanghai 201800, China

Keywords KB mirror · Beam size measurement · Beam diagnostic · Emittance · Synchrotron radiation

1 Introduction

The demand for highly brilliant X-ray synchrotron radiation (SR) motivates designers to produce low-emittance electron beams. High-energy photon source is a 6 GeV light source with a circumference of approximately 1300 m and is going to be built in Beijing, China [1]. This future light source, with a multiple-bend achromat lattice design for constructing a so-called diffraction-limited storage ring, is expected to achieve an ultralow emittance of 60 pm rad [2]. As an R&D project for HEPS, the HEPS test facility was established in 2016 to resolve key issues in accelerator physics and technology. Measuring the electron beam emittance is one of the most important issues to resolve for HEPS. Beam size measurement is generally used to obtain the emittance and the coupling. To this end, we proposed a Kirkpatrick–Baez (KB) mirror imaging method to measure the horizontal and vertical beam sizes, which are both approximately 5–10 µm. Here, we present the test KB beam size monitor, which was designed and tested specifically for the Shanghai Synchrotron Radiation Facility (SSRF) storage ring to measure a beam size of approximately 78 µm (RMS) (horizontal) and 20 µm (RMS) (vertical).

We compared some beam size measurement methods that can be roughly classified as imaging methods and interferometry methods. Imaging methods include visible light imaging [3], X-ray pinhole imaging [4, 5], X-ray imaging with a KB mirror [6], the use of Fresnel zone plates [7], the use of compound refractive lenses [8], and also X-ray coded-aperture imaging [9]. Interferometry methods include visible light double-slit interferometry [10, 11], the π polarization method [12], and X-ray Fresnel diffractometry [13]. Each type of monitor has advantages but also limitations. The X-ray pinhole camera is widely used for its simple setup and high practical reliability. The resolution of pinhole optics is a trade-off between the diffraction limit (hole too small) and geometric blurring (hole too large). Therefore, it is difficult to find much room to improve the resolution. The typical resolution of X-ray pinhole cameras is greater than 10 μm. The KB mirror monitor does not have this limitation, and it has some specific advantages. First, it has no chromatic aberration; therefore, it is not necessary to use a monochromator, and a higher flux is obtained, resulting in a higher signal-to-noise ratio. Second, the KB mirror can operate in the hard X-ray region, so diffraction makes a smaller contribution to the spatial resolution. Further, it can acquire a direct image of an electron beam, which can provide considerable information on the beam. Not only can the beam size in both directions be acquired, but also the operator can easily observe the beam motion, broadening, or tilt status.

2 Beamline design

2.1 SSRF storage ring and its parameters

The SSRF is a third-generation synchrotron light source operating at 3.5 GeV and located in Shanghai in China. It has been open to users since 2009 and serves 13 beamlines with nine insertion devices. The basic parameters of the ring are listed in Table 1. The SSRF has two diagnostic beamlines, both of which are extracted from the second dipole in the first cell. One beamline is at the 3° end and is used for visible light diagnostics, whereas the other, at the 0.8° end, is used for X-ray pinhole imaging. The pinhole in the X-ray pinhole camera system, which has a magnification of 1.5, is located in air; therefore, it is possible to install the KB mirror chamber between the pinhole and the X-ray camera.

Table 1 Basic parameters of the SSRF storage ring

Parameters	Value
Beam energy (GeV)	3.5
Beam current (mA)	200–300
Circumference (m)	432
RF frequency (MHz)	499.654
Natural emittance (nm rad)	3.9
Magnetic field of dipole (T)	1.2726
Critical photon energy (keV)	10.4
Horizontal RMS beam size (μm)	78
Vertical RMS beam size (μm)	20

2.2 Kirkpatrick–Baez mirror

In 1948, Kirkpatrick and Baez [14] first designed a system of two crossed spherical mirrors to eliminate the astigmatism of a single mirror used at glancing incidence. This method essentially eliminates the astigmatism and would eliminate spherical aberration using 1:1 imaging when the object and image both lie on the Rowland circle of the mirror. Hence, the residual aberration is the only factor limiting the resolution. The focusing equation of the two mirrors is $1/p + 1/q = 1/f = R\sin\theta$, where p is the object distance, q is the image distance, f is the focal length, R is the radius of curvature, and θ is the grazing incidence angle.

We use 1:1 imaging in our KB system with two cylindrical mirrors. The front mirror, which is placed horizontally, is called the vertical focusing mirror (VFM), and the back mirror, which is placed vertically, is called the horizontal focusing mirror (HFM). The parameters are shown in detail in Table 2. Both mirrors are fabricated by Thales SESO and a ZYGO interferometer is used to measure the slope error and radius of curvature. Three lines (− 5 mm, center, + 5 mm) are measured in each mirror with a frame. For the VFM, the average RMS slope error is 0.293 μrad, and the radius of curvature is 2.599 km. For the HFM, the average RMS slope error is 0.381 μrad, and the radius of curvature is 2.55 km.

Table 2 Designed KB mirror parameters

	VFM	HFM
Shape	Cylindrical	Cylindrical
Radius of curvature (km)	2.57	2.57
Grazing angle (mrad)	3	3
Substrate	Silicon	Silicon
Coating	Rh	Rh
Acceptance angle (μrad)	122	117
Size (L × W × H) (mm^3)	320 × 40 × 40	320 × 40 × 40
Clear aperture (L × W) (mm^2)	300 × 10	300 × 10
RMS roughness (nm)	< 0.2	< 0.2
RMS slope error (μrad)	< 0.3	< 0.3
Distance to source (m)	7.36	7.72
Distance to image (m)	8.08	7.72
Magnification	1.1	1
Hitting power (W)	1.083	0.251
Absorbed power (W)	0.832	0.058

Because of the reflective optics design, there is no chromatic aberration in the KB optics. According to an analysis by Susini and Wulff [15], the third-order spherical aberration, first-order coma, and third-order coma are the main aberrations contributing to focus broadening. In purely geometrical terms, the spot size can be expressed as follows [16]:

$$F = \frac{3}{16}L^2\frac{\theta_i}{p}\frac{1-M^2}{M} + S_Z M + S_Z(M+1)\frac{L}{4p}, \quad (1)$$

where F is the full width at half-maximum (FWHM) focus size, L is the illuminated length on the mirror, $M = q/p$ is the magnification, θ_i is the grazing angle, and S_z is the vertical source size; p and q are the source–mirror and mirror–focus distances, respectively. The first term corresponds to the third-order spherical aberration, and the two other terms of Eq. (1) are related to the first-order coma and third-order coma. As $M \approx 1$ in this case, there is no spherical aberration. Coma becomes the major contribution, which can also be ignored after the calculation because it broadens the FWHM focus size by no more than 2%. Thus, the optical aberrations are not included in the derivation of the point spread function (PSF).

2.3 System layout

A schematic of the KB mirror monitor layout is shown in Fig. 1. SR coming from the dipole first crosses a 1-mm-thick and 2-mm-diameter aluminum window at the front end, which defines the X-ray open angle as 0.35 mrad. The Al window acts as a filter and is used to isolate the vacuum from air; the lower photon energy cutoff is 10 keV. The KB mirror pair is located in an independent vacuum chamber to prevent oxidation, with two entrance slits on its upstream end that define the system's angular acceptance. To isolate the system from any significant low-frequency vibration, the mirrors are fixed on a $518 \times 712 \times 857\ \mathrm{mm}^3$ granite block by a UHV adjustment mechanism. The HFM is located equidistant between the source and image for one-to-one imaging; further, the magnification of the VFM is 1.1. In front of the entrance slits, a Cu attenuator is used both to attenuate the photon flux and to protect the mirrors from the long-term high heat load during operation.

To achieve better spatial resolution, we set our KB mirror to operate in the hard X-ray region to decrease the diffraction. The targeting source size is 20 μm (vertical) and 78 μm (horizontal). To set the dipole source point as the zero position, the VFM and HFM are located at 7.36 and 7.72 m, respectively, to make an image 15.44 m from the source. The mirror substrate is Si coated with Rh. Both mirrors have a 3 mrad grazing incidence angle, and most of the hard X-rays above 23.5 keV are absorbed by the first mirror. With the $V122$ μrad × $H117$ μrad acceptance angle calculated for the lengths of the two mirrors, the heat load at the first mirror is 1.083 W at a 300 mA beam current; 0.832 W is absorbed and would be removed by water cooling, and 0.251 W is reflected to the second mirror.

Figure 2 shows the spectrum of the SR after it is filtered by the Al window and limited by the aperture slits; the SR has a spectrum from approximately 12 to above 60 keV and peaks around 24 keV. After the VFM and HFM, the narrowed spectrum is from 12 to 23.5 keV and peaks around 20.5 keV.

2.4 Detector

We use two X-ray scintillator cameras to acquire a two-dimensional image of the beam profile; the cameras can be

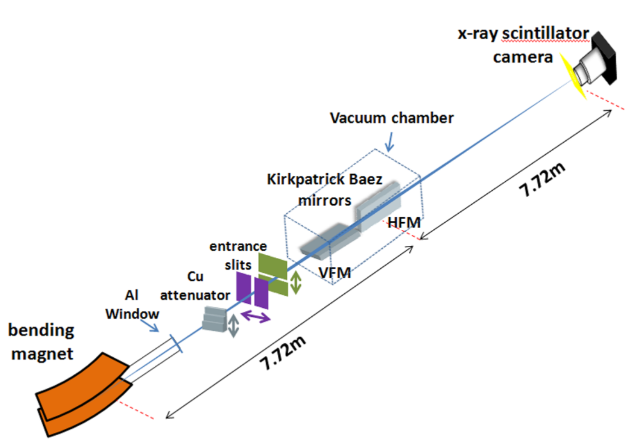

Fig. 1 (Color online) Schematic diagram of KB mirror system

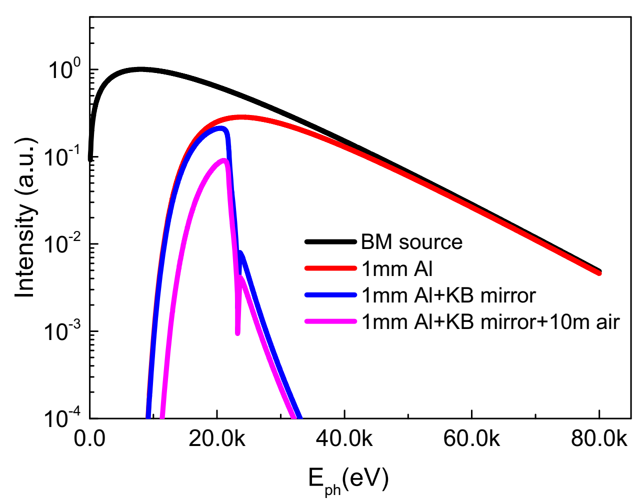

Fig. 2 (Color online) Spectrum of the SR from the bending magnet source as filtered by the Al window, KB mirror, and approx. 10 m of air

interchanged with each other by using motorized translation stages.

The first X-ray camera (cam1) is the original camera used as the detector in the X-ray pinhole system [17]. It has a 400-μm-thick YAG/Ce scintillator, which converts X-rays into visible light at a peak wavelength of 530 nm; visible light is reflected 90° by a flat mirror. A macro lens (Componon 2.8/50 from Schneider–Kreuznach) is used to image the screen of a compact IEEE 1394 CCD camera (AVT Guppy F-080B, pixel size 4.65 μm) with a magnification of 2. An application based on LabVIEW and a shared memory IOC core technique was developed to control the camera and communicate with the control system through the EPICS CA protocol.

The second camera (cam2) is an updated X-ray camera. It has better resolution using a 5-μm-thick LuAG/Ce crystal. The scintillator is a 10×0.005 mm^2 LuAG/Ce crystal produced by Crytur and glued onto a quartz substrate. A microscope connected to a CCD camera is used to view the image on the scintillator. To prevent hard X-rays from impinging on the CCD camera, visible light is reflected at 90° by a flat mirror. The CCD camera (Kodak full-frame KAF-8300) has a pixel size and spatial resolution of 5.4 μm, and the total number of pixels is 3358×2536. With $20 \times$ magnification microscope objectives, the effective pixel size is 0.27 μm. A Jima X-ray test by Crytur proved that the spatial resolution was better than 1.5 μm (Fig. 3). A control software package from Crytur is used to acquire images and control the focus.

3 Point spread function (PSF)

The accuracy of the KB mirror monitor is determined by the RMS PSF. The obtained image on the camera is the convolution of the source profile with the PSF of the entire system, which includes several independent terms: the PSF of the diffraction, the PSF of the X-ray camera, and the image blur caused by the mirror slope error. We calculate

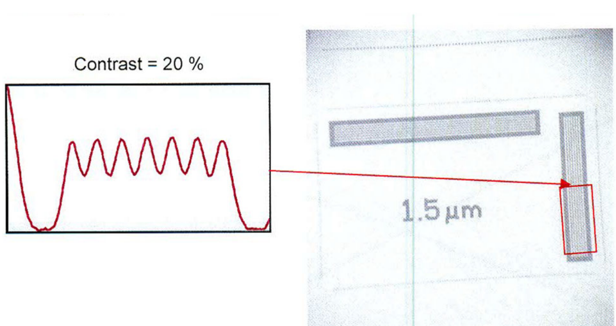

Fig. 3 (Color online) Result of spatial resolution test of cam2

the PSF assuming that the source and the PSF are Gaussian. Let us denote the RMS Gaussian size of the image as Σ; then it can be expressed as follows:

$$\begin{aligned}\Sigma^2 &= (\sigma \times M)^2 + S_{\text{diff}}^2 + S_{\text{slope}}^2 + S_{\text{camera}}^2 \\ &= (\sigma \times M)^2 + S_{\text{sys}}^2,\end{aligned} \quad (2)$$

where σ is the RMS size of the image of the photon source at the bending magnet, M is the magnification of the KB mirror, S_{diff} is the diffraction introduced by the aperture, S_{slope} is the RMS image blur induced by the mirror slope error, S_{camera} is the RMS spatial resolution of the X-ray camera, and S_{sys} is the effective RMS PSF of the entire system.

3.1 Diffraction limit

To calculate the image smear induced by aperture diffraction, a Gaussian is force-fitted to the diffraction pattern of a circular or rectangular aperture, and the width of the Gaussian is treated as a smearing term, S_{diff}, to be taken in quadrature with the beam size [18]. In this case,

$$S_{\text{diff}} \approx 0.4 \frac{\lambda}{2NA}, \quad (3)$$

where NA is the numerical aperture, which specifies the light-gathering power of the imaging system and is the half-open angle of the aperture, and λ is the wavelength of the X-rays. We use a peak wavelength of 0.06 nm (20.5 keV) here for the calculation. There is a small difference in the aperture between the vertical direction and horizontal direction. Table 3 lists the crucial apertures that determine the X-ray entrance angle.

For the horizontal direction, the entrance angle is determined by the dissector slits, which can be switched between 450 and 900 μm. In our experiment, we always use 450 μm slits, so the entrance angle is 64.3 μrad. According to Eq. (3), the diffraction limit of the HFM is $S_{\text{diff}}^{\text{HFM}} \approx 0.37$ μm, which is proportional to λ.

For the vertical direction, the entrance angle is determined by the synchrotron light's vertical opening angle, σ_{SR}:

$$\sigma_{\text{SR}} = \frac{E_0}{E}\left(\frac{\lambda}{3\lambda_{\text{c}}}\right)^{1/2}, \quad (4)$$

where $E_0 = 0.51$ MeV is the electron rest mass energy; $E = 3.5$ GeV is the electron energy of the SSRF storage ring; and $\lambda_{\text{c}} = 0.326$ nm is the critical wavelength of the SSRF dipole. From Eqs. (3) and (4), the VFM diffraction limit can be expressed as

$$S_{\text{diff}}^{\text{VFM}} \approx 0.4 \frac{E}{E_0}(3\lambda_{\text{c}} \cdot \lambda)^{1/2} \propto \lambda^{1/2}. \quad (5)$$

Table 3 Crucial apertures in vertical and horizontal directions

	Vertical			Horizontal		
	Size	Distance	Aperture angle	Size	Distance	Aperture angle
Al window	2 mm	5.69 m	351 μrad	2 mm	5.69 m	351 μrad
Dissector slits	450 μm	7 m	64.3 μrad	450 μm	7 m	**64.3 μrad**
X-ray opening angle	–	–	**36.1 μrad@20.5 keV**	–	–	–
Mirror aperture	300 mm	7.36 m	122 μrad	300 mm	7.72 m	117 μrad

Bold values indicate the smallest aperture angle that limit the entrance X-ray radiation

The calculated value is $S_{\mathrm{diff}}^{\mathrm{VFM}} \approx 0.66$ μm, which is proportional to $\lambda^{1/2}$.

3.2 Slope error

Short-length-scale variations from an ideal mirror surface are referred to as surface roughness. The surface roughness of the mirror may affect its reflectivity. Long-length-scale deviations from an ideal mirror surface are referred to as slope errors. The slope error can be amplified by the mirror-to-image distance q when X-rays are reflected away from the surface. The image blur due to the slope error depends on the focal length of the mirror and the RMS slope error: $S_{\mathrm{slope}} = 2 \times \sigma_{\mathrm{slope}} \times q$, where σ_{slope} is the RMS slope error. Figure 4 shows the RMS slope error of the mirror centerline measured by the ZYGO interferometer. Table 4 shows the average RMS slope error of the center line, + 5 mm line, and − 5 mm line, and the calculated image blur of the VFM and HFM.

3.3 Camera resolution

To measure the PSF of the X-ray camera composed of a scintillator screen, macro lens, and camera, we used an opaque mask to cover the left part of the screen in front of the X-ray camera. The opaque mask, which has a sharp edge, is made of a tungsten bar. Figure 5 shows the measurement results of cam1 and cam2 in our system. Cam2 has a greatly improved resolution of 1.53 μm. Table 5 summarizes the results.

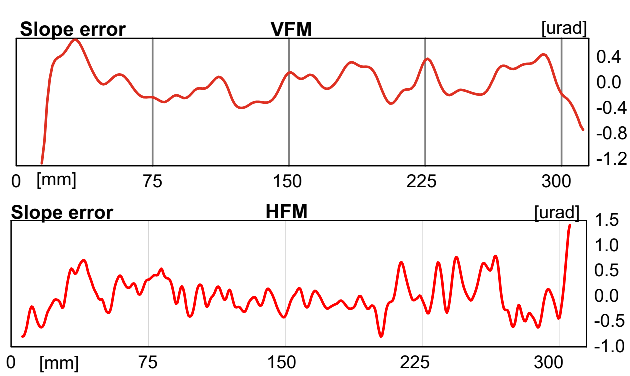

Fig. 4 (Color online) Slope error of the centerline of the VFM (top) and HFM (bottom)

3.4 System PSF evaluation

In this section, we briefly summarize the total width of the PSF S_{sys} of the KB system. It is calculated by using the quadratic sum of all the terms. The diffraction limit item is in the submicron range, and the slope error term is 4.69 μm for the VFM and 5.87 μm for the HFM. Table 6 summarizes the PSF in the vertical and horizontal directions for different scintillator cameras. It shows that when cam1 is used, the camera resolution is the dominant term, contributing the largest component to the image extension. After installation of the updated camera, cam2, with 1.5 μm resolution (which can be interchanged with cam1), the largest contribution becomes the slope error term. It is obvious that a smaller PSF width is better. Nevertheless, deconvolution can easily be done by quadratic subtraction, as given by Eq. (2) when the PSF is below the beam size to be measured. To obtain the image size with an error of less than 10%, the distortion S_{sys} should be less than half the beam size; hence, for our system, a beam size of $\sim$ 10 μm can be measured directly using cam2.

4 Experimental results

4.1 Beam size measurement

Here we present measurements of the electron beam size by cam1 in top-up mode at a 240 mA beam current (Fig. 6, data from July 20, 2017). The transverse beam size was $\Sigma_x = 77.5$ μm (horizontal) by $\Sigma_y = 34.3$ μm (vertical), as obtained from the CCD camera output before PSF calibration. After PSF calibration using the data in Table 6, the beam size is found to be $\sigma_x = 74.7$ μm and $\sigma_y = 25.1$ μm.

Table 4 Measured average RMS slope error and calculated image blur

	Slope error (σ_{slope})	Mirror-to-image distance (q)	Blur function (S_{slope})
VFM	0.29 μrad	8.08 m	4.69 μm
HFM	0.38 μrad	7.72 m	5.87 μm

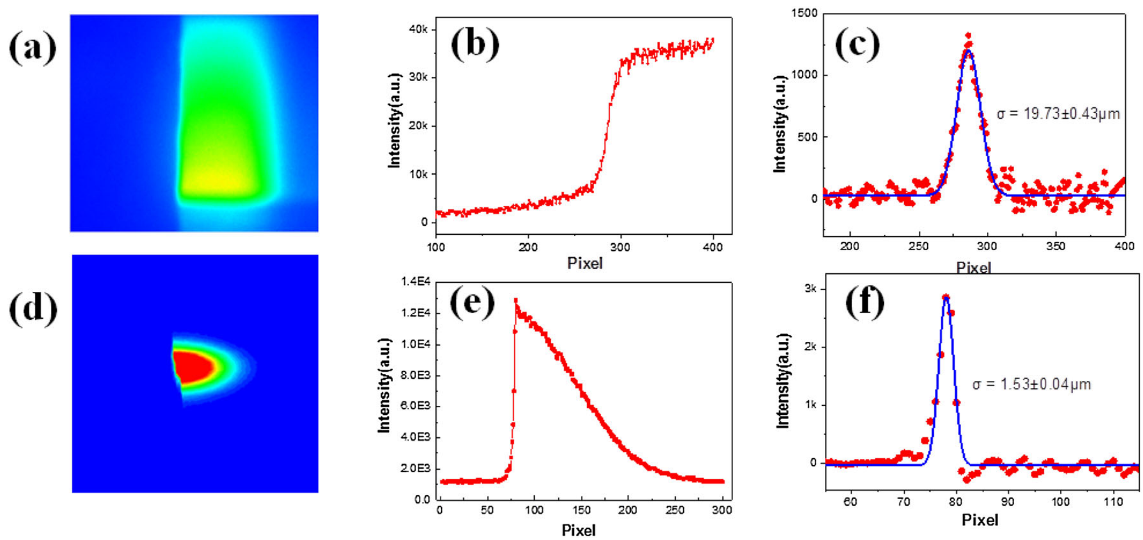

Fig. 5 (Color online) **a** Image of tungsten bar edge observed in X-ray fan by cam1. **b** Profile of the edge in (**a**). **c** Derivative of the profile in (**b**) (red) and a fitted Gaussian curve (blue). **d** Image of tungsten bar edge observed in a KB mirror image by cam2. **e** Profile of the edge in (**d**). **f** Derivative of the profile in (**e**) (red) and a fitted Gaussian curve (blue)

Table 5 Parameters and measured resolution of the two cameras

Camera	Scintillator	Thickness	Magnification	Pixel size	Pixel binning	Resolution
Cam1	YAG/Ce	400 μm	2	4.65 μm	1 × 1	19.73 ± 0.43 μm
Cam2	LuAG/Ce	5 μm	20	5.4 μm	4 × 4	1.53 ± 0.04 μm

Table 6 Calculated PSF of the KB system in vertical and horizontal directions

	S_{diff}	S_{slope}	S_{camera}		S_{sys}
Vertical	0.66 μm	4.69 μm	Cam1	19.73 μm	20.29 μm
			Cam2	1.53 μm	4.97 μm
Horizontal	0.37 μm	5.87 μm	Cam1	19.73 μm	20.59 μm
			Cam2	1.53 μm	6.08 μm

4.2 Beam-based calibration

To evaluate the online PSF for cam1, a beam-based calibration method [19] was used. We gradually changed the horizontal beam size σ_x at the source point by modifying the power supply current I_{Q5} of the fifth set of quadrupoles and measured the image size Σ_x at each I_{Q5} setting. It is obvious that σ_x is what we want to acquire from Σ_x by quadratic subtraction, as given by Eq. (2), with a correct PSF width S_{sys}. However, we can use a model horizontal beam size σ_x^{model}, which can be calculated using linear optics from closed orbits (LOCO), to evaluate the PSF.

After the linear optics measurements and the optimization procedure using LOCO, the maximum beta function beating of the SSRF storage ring was minimized to less than 1%. In this case, the difference in the beam parameters between the model and the practical machine is also smaller than 1%. The model horizontal beam size σ_x^{model} is calculated by

$$\sigma_x^{model} = \sqrt{\beta_x \varepsilon_x + (\eta_x \sigma_e)^2}, \tag{6}$$

where β_x and η_x are the betatron and dispersion functions at the source point and in the horizontal plane, respectively, and ε_x and σ_e are the horizontal emittance and relative energy spread of the electron beam, respectively. The machine parameters and measurement values are shown in detail in Table 7.

To determine the PSF, a least-square linear fitting method is used to fit the squares of Σ_x and σ_x^{model} with

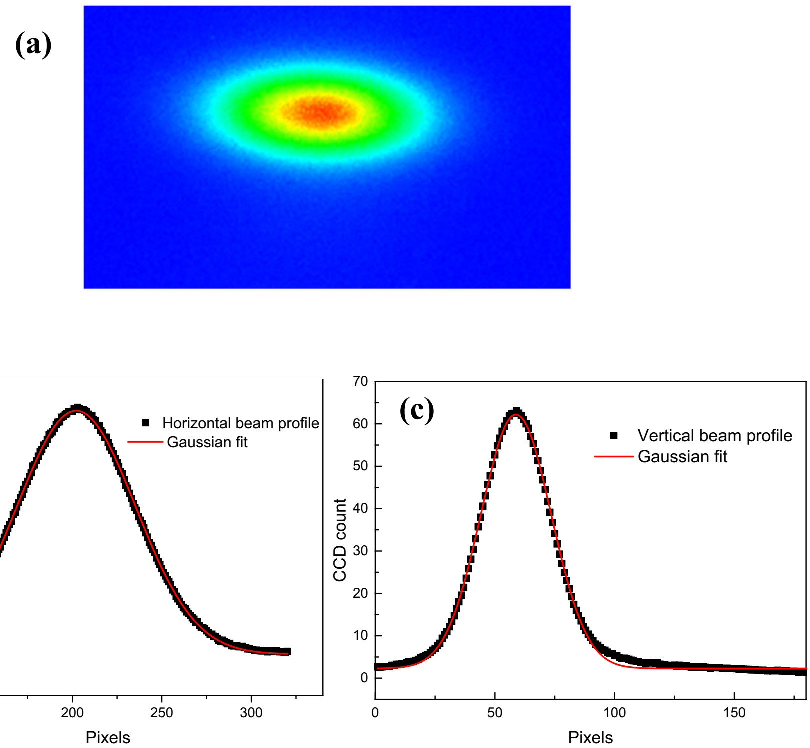

Fig. 6 (Color online) **a** Observed image of the KB mirror monitor in the SSRF control room. **b** Horizontal and **c** vertical beam profiles with their fitted Gaussian curves

Table 7 Theoretical horizontal beam sizes and the corresponding image sizes obtained for various machine parameters

I_{Q5} (ratio)	ε_x (nm rad)	σ_e	β_x (m)	η_x (m)	σ_x^{model} (μm)	Σ_x (μm)
92%	8.538	0.9827×10^{-3}	1.0998	0.0998	137.9	134.5
93%	7.094	0.9828×10^{-3}	1.0426	0.0901	123.4	122.8
94%	6.027	0.9828×10^{-3}	0.9907	0.0818	111.5	112.6
95%	5.250	0.9828×10^{-3}	0.9432	0.0746	101.6	103.9
96%	4.699	0.9828×10^{-3}	0.8995	0.0682	93.4	97.7
97%	4.327	0.9828×10^{-3}	0.8589	0.0626	86.6	90.6
98%	4.100	0.9828×10^{-3}	0.8210	0.0576	81.0	85.2
99%	3.992	0.9828×10^{-3}	0.7855	0.0531	76.5	81
100%	3.983	0.9828×10^{-3}	0.7521	0.0490	72.9	77.7
101%	4.059	0.9828×10^{-3}	0.7204	0.0453	70.1	74.9
102%	4.209	0.9828×10^{-3}	0.6902	0.0420	67.9	72.6
103%	4.423	0.9828×10^{-3}	0.6615	0.0389	66.3	71
104%	4.696	0.9828×10^{-3}	0.6339	0.0361	65.1	69.8
105%	5.024	0.9828×10^{-3}	0.6075	0.0335	64.3	68.8
106%	5.403	0.9828×10^{-3}	0.5819	0.0311	63.9	68.3
107%	5.833	0.9828×10^{-3}	0.5572	0.0289	63.7	67.9

Eq. (2) at each I_{Q5} setting, where the fitting slope is set to 1 (Fig. 7). The fitting value is $S_{sys} = 21.9 \pm 2.5$ μm. It is in good agreement with the off-line calculated value of 20.59 μm in Table 6. Figure 8 compares the model theoretical value and measurement value of the beam size with online PSF calibration. The measurement value is in good agreement with the theoretical value.

4.3 High-resolution camera imaging results

On January 18, 2018, the new LuAG/Ce camera (cam2) was installed next to the original YAG/Ce camera (cam1) so that both cameras can be used by changing their position using motorized translation stages. Both the Jima X-ray test by Crytur and the slanted edge test at the diagnostic beamline (see Sect. 3.3 for details) demonstrated very good

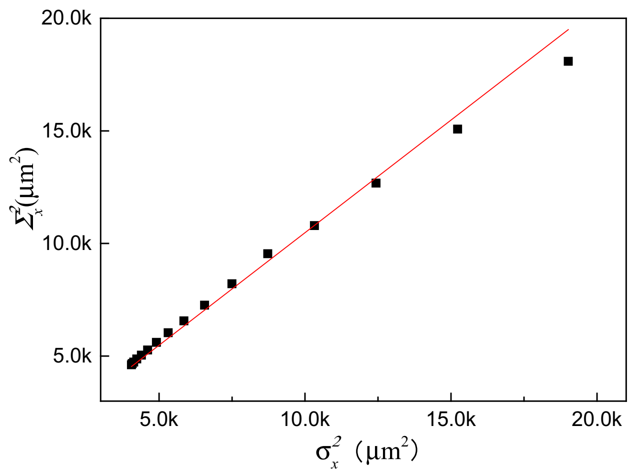

Fig. 7 Least-square linear fitting of the squares of Σ_x and σ_x^{model}

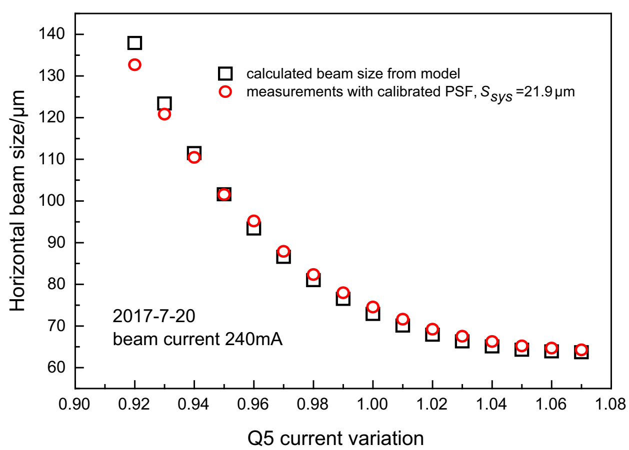

Fig. 8 (Color online) Comparison of theoretical beam size and measured beam size with online calibrated PSF

performance, indicating that the spatial resolution was approximately 1.5 μm.

Figure 9 shows the imaging results of the two cameras. It is obvious that cam2 shows the focal image better. After a Gaussian fit of the raw data, the transverse beam sizes from cam1 are $\Sigma_x^{cam1} = 81.1$ μm, $\Sigma_y^{cam1} = 35.0$ μm, whereas the data from cam2 are $\Sigma_x^{cam2} = 71.5$ μm, $\Sigma_y^{cam2} = 28.6$ μm. Cam2 shows greatly decreased image blur, as we expected.

5 Conclusion

In this paper, we presented the KB mirror beam size monitor with a bending magnet source at the SSRF. It can be interchanged with the original X-ray pinhole monitor. We evaluated the PSF of the system by calculating each term that could cause image blur. Further, a beam-based calibration experiment was done to determine the PSF with the original camera. The experimental PSF result is in good agreement with the calculated data.

A new X-ray camera with a 5-μm-thick LuAG/Ce scintillator was installed. It has a resolution of approximately 1.5 μm. A comparison of beam images obtained by the two cameras shows that the new camera has greatly decreased image blur. The calculated PSF of the KB mirror monitor with the new camera is 4.97 μm vertically and 6.08 μm horizontally, and slope error-induced image broadening is the major contribution. The current state-of-the-art KB mirror, offered by J-Tec (Osaka, Japan) and fabricated by the elastic emission machining technique, can achieve an RMS slope error of less than 0.05 μrad and a figure accuracy of $<$ 1 nm in a 350-mm-long mirror [20]. Therefore, the PSF can likely be further improved by using a pair of KB mirrors with lower slope error.

References

1. G. Xu, X.H. Cui, Z. Duan et al., Progress of the lattice design and physics studies on the high energy photon source, in *Proceedings of IPAC2017,* Copenhagen, Denmark, 2017, pp. 2697–2699
2. Y. Jiao, G. Xu, Optimizing the lattice design of a diffraction-limited storage ring with a rational combination of particle swarm and genetic algorithms. Chin. Phys. C **41**, 027001 (2017). https://doi.org/10.1088/1674-1137/41/2/027001
3. J.W. Flanagan, S. Hiramatsu, T. Mitsuhashi, Optical beamlines for the KEKB-factory synchrotron radiation monitors, in *Proceedings of PAC1999*, New York, USA, 1999, pp. 2120–2122

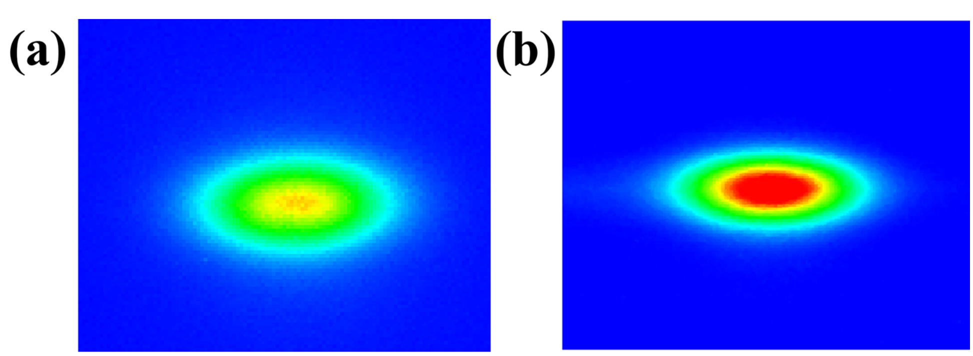

Fig. 9 (Color online) Images of the beam profile from cam1 **a** and cam2, **b** taken on January 1, 2018

4. P. Elleaume, C. Fortgang, C. Penel et al., Measuring beam sizes and ultra-small electron emittances using an X-ray pinhole camera. J. Synchrotron Rad. **2**, 209–214 (1995). https://doi.org/10.1107/S0909049595008685
5. C. Thomas, G. Rehm, I. Martin et al., X-ray pinhole camera resolution and emittance measurement. Phys. Rev. Spec. Top. Accel. Beams **13**, 022805 (2010). https://doi.org/10.1103/PhysRevSTAB.13.022805
6. T.R. Renner, H.A. Padmore, R. Keller, Design and performance of the ALS diagnostic beamline. Rev. Sci. Instrum. **67**, 3368 (1996). https://doi.org/10.1063/1.1147369
7. H. Sakai, M. Fujisawa, K. Iida et al., Improvement of Fresnel zone plate beam-profile monitor and application to ultralow emittance beam profile measurements. Phys. Rev. Spec. Top. Accel. Beams **10**, 042801 (2007). https://doi.org/10.1103/PhysRevSTAB.10.042801
8. G. Kube, J. Gonschior, U. Hahn et al., PETRA III diagnostics beamline for emittance measurements, in *Proceedings of IPAC*2010, Kyoto, Japan, 2010, pp. 909–911
9. J. Flanagan, K. Kanazawa, J. Alexander et al., Performance of coded aperture X-ray optics with low emittance beam at CESRTA, in *Proceedings of PAC09,* Vancouver, BC, Canada, 2010, pp. 3561–3563
10. T. Mitsuhashi, Spatial coherency of the synchrotron radiation at the visible light region and its application for the electron beam profile measurement, in *Proceedings of PAC1997*, Vancouver, BC, Canada, 1997, pp. 766–768
11. S.T. Wang, D.L. Rubin, J. Conway et al., Visible-light beam size monitors using synchrotron radiation at CESR. Nucl. Instrum. Methods Phys. Res. A **703**, 80–90 (2013). https://doi.org/10.1016/j.nima.2012.11.097
12. J. Breunlin, Å. Andersson, N. Milas et al., Methods for measuring sub-pm rad vertical emittance at the Swiss Light Source. Nucl. Instrum. Methods Phys. Res. A **803**, 55–64 (2015). https://doi.org/10.1016/j.nima.2015.09.032
13. M. Masaki, S. Takano, M. Takao et al., X-ray fresnel diffractometry for ultralow emittance diagnostics of next generation synchrotron light sources. Phys. Rev. Spec. Top. Accel. Beams **18**(4), 042802 (2015). https://doi.org/10.1103/PhysRevSTAB.18.042802
14. P. Kirkpatrick, A.V. Baez, Formation of optical images by X-rays. J. Opt. Soc. Am. **38**, 766–774 (1948)
15. J. Susini, M. Wulff, Study of design parameters governing the performances of synchrotron mirrors. High Heat Flux Eng. **II**(1997), 278–290 (1993)
16. J. Susini, Design parameters for hard X-ray mirrors: the European synchroton radiation facility case. Opt. Eng. **34**, 361–377 (1995). https://doi.org/10.1117/12.194835
17. G.Q. Huang, J. Chen, Z.C. Chen et al., X-ray pinhole camera system design for SSRF storage ring. Nucl. Tech. **33**, 806–809 (2010). **(in Chinese)**
18. J.W. Flanagan, Diagnostics for ultra-low emittance beams, in *Proceedings of IPAC2011*, San Sebastián, Spain, 2011, pp. 1959–1963
19. Y.B. Leng, G.Q. Huang, M.Z. Zhang et al., The beam-based calibration of an X-ray pinhole camera at SSRF. Chin. Phys. C **36**, 80–83 (2012). https://doi.org/10.1088/1674-1137/36/1/014
20. S.G. Alcock, K.J.S. Sawhney, S. Scott et al., The Diamond-NOM: a non-contact profiler capable of characterizing optical figure error with sub-nanometre repeatability. Nucl. Instrum. Methods Phys. Res. A **616**, 224–228 (2010). https://doi.org/10.1016/j.nima.2009.10.137